PAPER

Accurate Image Separation Method for Two Closely Spaced Pedestrians Using UWB Doppler Imaging Radar and Supervised Learning

Kenshi SAHO[†a], *Member*, **Hiroaki HOMMA**[†*], *Nonmember*, **Takuya SAKAMOTO**[†], *Member*, **Toru SATO**[†], *Fellow*, **Kenichi INOUE**[††], *and* **Takeshi FUKUDA**[††], *Members*

SUMMARY Recent studies have focused on developing security systems using micro-Doppler radars to detect human bodies. However, the resolution of these conventional methods is unsuitable for identifying bodies and moreover, most of these conventional methods were designed for a solitary or sufficiently well-spaced targets. This paper proposes a solution to these problems with an image separation method for two closely spaced pedestrian targets. The proposed method first develops an image of the targets using ultra-wide-band (UWB) Doppler imaging radar. Next, the targets in the image are separated using a supervised learning-based separation method trained on a data set extracted using a range profile. We experimentally evaluated the performance of the image separation using some representative supervised separation methods and selected the most appropriate method. Finally, we reject false points caused by target interference based on the separation result. The experiment, assuming two pedestrians with a body separation of 0.44 m, shows that our method accurately separates their images using a UWB Doppler radar with a nominal down-range resolution of 0.3 m. We describe applications using various target positions, establish the performance, and derive optimal settings for our method.

key words: human imaging, closely-spaced pedestrians, image separation, UWB Doppler radar, supervised learning, support vector machine (SVM)

1. Introduction

The imaging and identification of moving bodies using radar is a promising option for security systems. For such applications, a simple, accurate feature extraction of the detected targets is needed. Low-complexity radar systems using micro-Doppler radars have been proposed for this purpose [1]–[8]. These systems achieve intruder detection and motion classification based on time-frequency micro-Doppler signatures. However, the primary aim of these systems is detection or classification, and acquiring further details of location, shape, and motion is difficult. Moreover, most of these conventional methods were designed for a single human target. Although conventional pulse radar systems detect multiple targets using a simple peak detection method such as the CLEAN algorithm [9], [10], they can only be ap-

plied to sufficiently well-spaced targets. Bilik and Tabrikian [7] proposed a method for classifying whether one or two people are detected using the data of a low range resolution ground surveillance radar. However, its classification accuracy is inadequate for the identification of each person. To track multiple bodies in a realistic situation, Doppler radar interferometric imaging with a dual frequency continuous-wave signal has been proposed [11], [12]. This method separates multiple scatterers using differences in their micro-Doppler frequencies and estimates the trajectory of each separated scatterer with direction-of-arrival (DOA) estimation using interferometry. However, its range resolution is unsuitable for acquiring details of body shape and motion and yields many false images because of interference from multiple targets. Thus, the separation of closely spaced multiple bodies is also difficult using this method.

As a solution to these problems, ultra wide-band (UWB) radar is a powerful tool because of its high-resolution imaging capability. Although accurate imaging algorithms with UWB radar for a moving target have been proposed [13]–[16], they are not suitable for complex-shaped moving targets such as human bodies. To resolve this problem, we previously proposed an imaging method using UWB Doppler radar imaging [17], [18]. This method provides high-resolution images of multiple scattering centers using Doppler radar interferometric imaging methods and UWB signals. In addition, we proposed a method for rejecting false images caused by radar interference and achieved reliable, real-time pedestrian imaging and identification in a realistic environment [18]. However, the effectiveness of the proposed UWB Doppler imaging radar was only confirmed for a single human target; the separation and identification of more than one pedestrian was not considered.

This paper considers the separation of UWB Doppler radar images for two pedestrian targets where the minimum distance between them is smaller than the range resolution, a difficult task for conventional radar target separation methods. First, we introduce simple image separation methods using range profiles or an unsupervised classification method. We experimentally apply these methods to a group image estimated by UWB Doppler imaging radar and show that the separation accuracy of closely spaced pedestrians is unsatisfactory. To solve this problem, we propose

an accurate separation method using the supervised learning of radar images. We first propose a real-time training data extraction method based on range profiles. Next, we compare the separation accuracy of several representative supervised learning methods (k-nearest neighbor [5], [19], naive Bayesian classifier [7], [20], and support vector machine [6], [21], [22]) using extracted training data, and then select the most appropriate method. In addition, we propose a rejection method for false points existing around the separation plane. An experiment consisting of two close pedestrian targets showed that our proposed method separated their images accurately where the number of targets was assumed to be two. Moreover, applications with various target positions are described, their performance is established, and suitable settings for the proposed separation method are derived.

2. UWB Doppler Imaging Radar

2.1 System Setup

Figure 1 shows a schematic of the radar setup. We assume that the targets are two pedestrians, the nearer is denoted Target 1 and the further Target 2. This paper does not consider the situation where Target 2 overtakes Target 1, and assumes that the number of targets (two) is known. Note that the number of targets could be determined by other methods such as a multiple hypothesis tracker [10] or target number classification method [7], and this paper thus does not consider the target number estimation problem. A transmitting antenna and Receivers 1, 2, and 3 are set up in the $y = 0$ plane. The positions of the transmitting antenna and Receivers 1, 2, and 3 are expressed as $(x, z) = (d_h/2, d_v/2+z_c)$, $(-d_h/2, -d_v/2+z_c)$, $(d_h/2, -d_v/2+z_c)$, and $(-d_h/2, d_v/2+z_c)$, respectively. The receiving antenna pair of Receivers 1 and 2 constitutes a horizontal interferometer and the pair of Receivers 1 and 3 constitutes a vertical interferometer. Measurements are conducted for certain po-
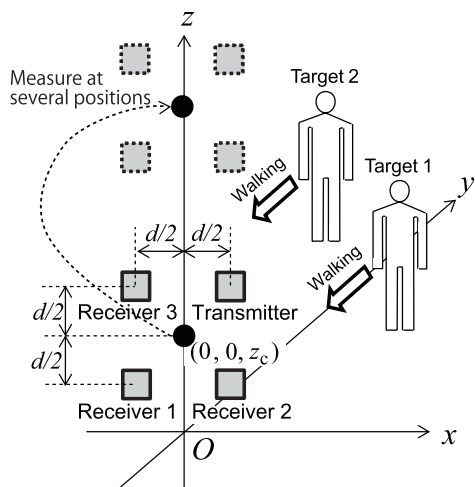

Fig. 1 System setup.

sitions and imaging results are acquired by the superposition of a result at each position z_c. The transmitting signal is a continuous wave (CW) signal with a frequency of f_0 modulated by an m-sequence of chip width t_C, giving a range resolution of $\Delta R = ct_C/2$ [24], [25], where c is the speed of light. The received signal waveform $s_{ik}(t)$ in range k using receiver i is acquired by taking a cross-correlation of the raw received signal with the time-shifted m-sequence [24].

2.2 Imaging Procedure

The UWB Doppler imaging radar separates multiple scattering centers in the frequency domain and estimates the positions of extracted scattering centers [17], [18]. If different scattering centers have different radial velocities, we can separate these by the differences in their Doppler frequencies. The Doppler frequency is expressed as:

$$f_d = \frac{2v_d}{\lambda}, \tag{1}$$

where v_d is the radial velocity and λ is the wavelength. The frequency f_d for each time instance is determined by a time-frequency analysis of the received signal. In this paper, a time-frequency distribution $S_{ij}(t, v_d)$ is obtained by a sliding-window discrete Fourier transform (SDFT) [23] of $s_{ij}(t)$ and is calculated by:

$$S_{ik}(t, v_d) = \int_{-\infty}^{\infty} s_{ik}(\tau)w_H(\tau - t)e^{-j4\pi v_d\tau/\lambda}d\tau, \tag{2}$$

where $w_H(t)$ is the Hamming window function, expressed as:

$$w_H(t) = \begin{cases} 0.54 - 0.46\cos\dfrac{2\pi}{T_w}t & (0 \le t \le T_w) \\ 0 & \text{(otherwise)}, \end{cases} \tag{3}$$

where T_w is the window size. The SDFT calculates Eq. (2) for all time bins. The significant peaks of $S_{ik}(t, v_d)$ are extracted, and these peaks correspond to the scattering centers from the time-frequency distribution.

We then estimate a position for each scattering center. The DOAs are estimated using interferometry, where the elevation DOA θ_{ELn} and azimuth DOA θ_{AZn} of the n-th scattering center are calculated from [11], [12]:

$$\theta_{EL}(t, v_{dn}) = \sin^{-1}\left[\frac{\angle S_{1k}(t, v_{dn}) - \angle S_{3k}(t, v_{dn})}{(2\pi d/\lambda)}\right], \tag{4}$$

$$\theta_{AZ}(t, v_{dn}) = \sin^{-1}\left[\frac{\angle S_{1k}(t, v_{dn}) - \angle S_{2k}(t, v_{dn})}{\{2\pi d\cos\theta_{EL}(t, v_{dn})/\lambda\}}\right], \tag{5}$$

where $\angle A$ is the phase of A and k is the range bin where target n is detected. The distance $R(t, v_{dn})$ is estimated by finding the range that maximizes the echo intensity using the range interpolation method [17]. With the acquired range and DOAs, the positions of the scattering centers $\mathbf{x}_s(t, v_{dn})$ are determined from:
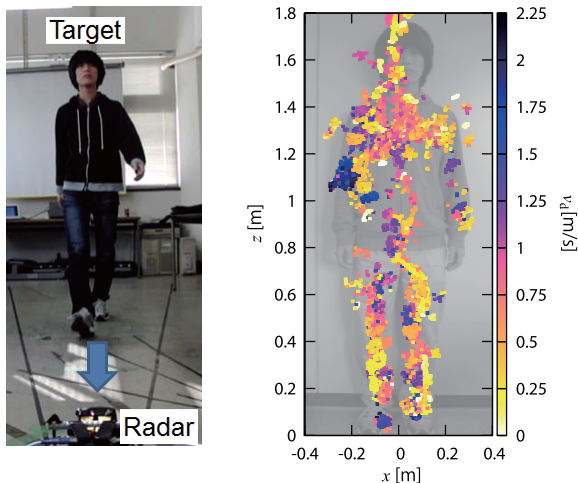
$$\mathbf{x}_s(t, v_{dn}) =$$

Fig. 2 Application example of the UWB Doppler imaging radar. Experimental site (left) and frontal view of the estimated scattering centers (right).

Fig. 3 Experimental setup with two pedestrian targets.

$$\begin{bmatrix} x_\text{s}(t, v_{\text{d}n}) \\ y_\text{s}(t, v_{\text{d}n}) \\ z_\text{s}(t, v_{\text{d}n}) \end{bmatrix} = \begin{bmatrix} R(t, v_{\text{d}n}) \cos\theta_{\text{EL}}(t, v_{\text{d}n}) \sin\theta_{\text{AZ}}(t, v_{\text{d}n}) \\ R(t, v_{\text{d}n}) \cos\theta_{\text{EL}}(t, v_{\text{d}n}) \cos\theta_{\text{AZ}}(t, v_{\text{d}n}) \\ R(t, v_{\text{d}n}) \sin\theta_{\text{EL}}(t, v_{\text{d}n}) + z_\text{c} \end{bmatrix}.$$

(6)

In addition, we apply a false image rejection method [17] to the estimated $\mathbf{x}_\text{s}(t, v_{\text{d}n})$ to reduce the effect of interference between multiple scattering centers.

Figure 2 illustrates the imaging result of a human target using the method described in [17]. In this example, with settings $d_\text{v} = d_\text{h} = 3.5$ cm, $f_0 = 26.4$ GHz and $W = 500$ MHz, a pedestrian is walking toward the transmitter. As shown in this result, a human outline is identifiable indicating that radar imaging achieves adequate outcomes. However, application to multiple targets was not previously considered. This paper is the first to consider the problem of separating two closely spaced pedestrian targets.

3. Simple Image Separation Methods and Their Problems

This section introduces two simple image separation methods for two targets and confirms their performance experimentally. One method separates the estimated scattering centers by identifying a delimiting boundary between the two targets using the range difference between targets and the other method uses cluster analysis of images.

3.1 Separation Method Based on Range Difference

3.1.1 Separation Procedure

This section investigates a simple target separation method using a delimiting boundary determined by the range difference between targets. Here, we extract the delimiting boundary as a power-weighted mean of the range profile for each time bin, expressed as:

$$B(t) = \sum_{j}^{N_\text{R}} j\Delta R |s_{1j}(t)|^2 (j\Delta R)^4 \Big/ \sum_{j}^{N_\text{R}} |s_{1j}(t)|^2 (j\Delta R)^4, \quad (7)$$

where N_R is the number of range bins. The factor with an exponent of four compensates for the range attenuation in the radar equation. A target label (Target 1 or 2) for each estimated scattering center is determined by comparison of $B(t)$ and $R(t, v_{\text{d}n})$.

3.1.2 Application Example with Experiment and Problem

This section describes an experiment where we imaged two pedestrians and determined the delimiting boundary from Eq. (5). Figure 3 shows a photograph of the setup. Two pedestrians walked in phase simultaneously with a gait cycle of 1.25 s and an average speed of 0.96 m/s. Target 1, 1.63 m tall, walked from $(x, y) = (0.25\,\text{m}, 3.9\,\text{m})$ to $(0.25\,\text{m}, 1.5\,\text{m})$ while Target 2, 1.75 m tall, walked from $(x, y) = (-0.2\,\text{m}, 4.35\,\text{m})$ to $(-0.2\,\text{m}, 1.95\,\text{m})$. The separation of their torsos was approximately 0.44 m. Considering the range spread of the target, this is a relatively difficult task for conventional UWB Doppler radar imaging techniques because the separation of the targets is not sufficient compared to the nominal range resolution of 0.3 m, and the echoes from many parts of the body of both targets were mixed in the same range bin. In addition, they walked in phase and in the same direction, a relatively tough situation to analyze because Doppler radar separates targets using motion difference.

The radar parameters were $d_\text{v} = 3.5$ cm, $d_\text{h} = 3$ cm, $f_0 = 26.4$ GHz, $W = 500$ MHz, and $\Delta R = 30$ cm. Horn antennas were used with a -3 dB beam-width of $\pm 11°$ in both the E- and H-planes. The interpulse period was 1.29 ms, and the window size for the SDFT was 165 ms. We took measurements at four antenna positions to acquire the data that corresponded to the whole body: $z_\text{c} = 0.36, 0.83, 1.3$, and 1.5 m, and imaging was performed by superposing the scattering centers estimated from each antenna location.
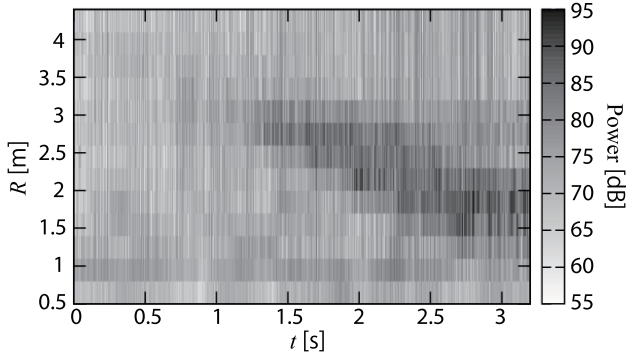
Fig. 4   Time-variation of the range profile for Rx_1 at z_c = 0.36 m.
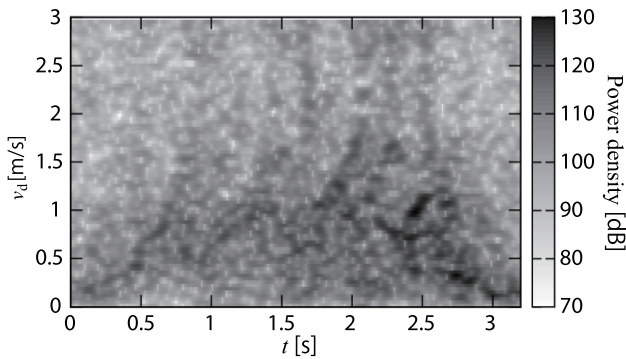

Fig. 5   Summation of spectrograms for range from Receiver 1 at z_c = 0.36 m.

Figure 4 shows the time-variation of the range profile for Receiver 1 at z_c = 0.36 m. The strong echoes are obtained for $t > 1.5$ s. We can verify from these echoes that both targets are walking at an approximately constant speed towards the antennas. Figure 5 shows the summation of the spectrograms for ranges corresponding to Fig. 4. The radial velocity offset corresponding to the walking speed and the micro-Doppler signatures of the leg motion are observed.

Figure 6 shows the top view of the imaging and separation results using the simple separation method. Here, we use the data for $t > 1.5$ s because of the signal-to-noise ratio. Many separation errors are obtained because the range difference between the targets is too small compared to ΔR. Figure 7 shows the front views of the images separated by the simple separation method for 1.76 s < t < 2.39 s, corresponding to a single stride or half a walking cycle. Although human features are discernible to a certain degree, the extraction of a human target is difficult because of the many separation errors.

3.2   Separation Using Cluster Analysis

Another approach considered here is cluster analysis of image. This section investigates the separation performance of the k-means method that is a representative cluster analysis method [26]. The feature vector is composed of the *xyt* of the estimated scattering centers because pedestrian targets are assumed, where the height differences (in the z-axis
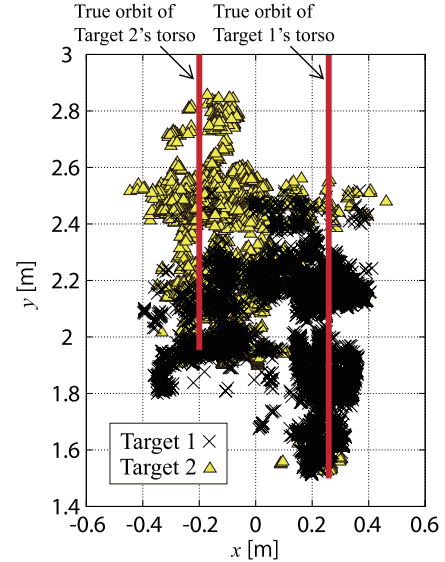

Fig. 6   Top view of the image separation result using the simple method.

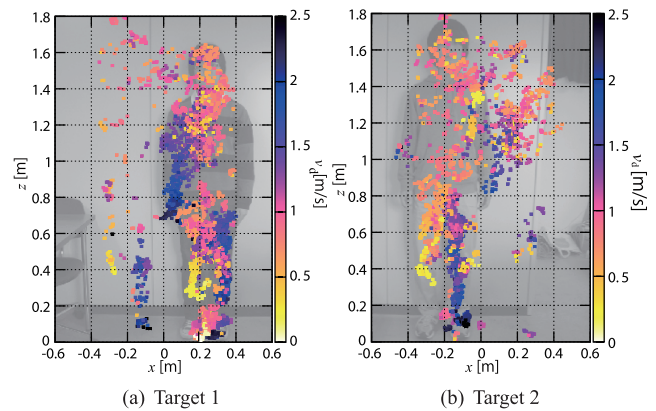(a) Target 1   (b) Target 2

Fig. 7   Frontal view of the image separated by the simple method based on range difference.

direction) among targets are not clear. The Euclidian distance for the k-means method between the i-th feature vector (x_{si}, y_{si}, t_i) and the mean point of the j-th class (x_{mj}, y_{mj}, t_{mj}) is expressed as [26]

$$D_{sm} = \sqrt{(x_{si} - x_{mj})^2 + (y_{si} - y_{mj})^2 + (t_i - t_{mj})^2}. \quad (8)$$

Figure 8 shows the separation result with the k-means method for $k = 2$ using the same data of Fig. 6. As shown in this figure, the separating of estimated image points almost failed. This is because accurate separation using a k-means method is realized only for data with a clear boundary, and these estimated images do not have one. Moreover, the k-means method does not use prior knowledge of the target features. Therefore, accurate separation using this method is difficult. Additionally, results using other cluster analysis methods such as Ward's method [27] were almost the same as the k-means method. Thus, image separation using a cluster analysis approach is difficult for closely spaced pedestrians.
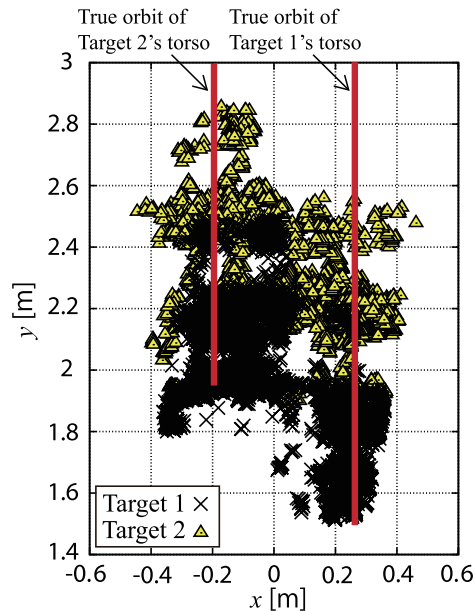
Fig. 8 Top view of the image separation result using the k-means method.

Fig. 9 An example of range profile and threshold for training data acquisition.

4. Image Separation Using a Supervised Learning Method

To achieve accurate separation, supervised learning methods are our approach of choice because they can realize more accurate classification/separation than cluster analysis techniques thanks to the use of training data. However, it is difficult for the UWB Doppler radar imager to prepare the appropriate training data in advance. This is because the radar parameters, such as the positions of scattering centers, Doppler frequency, and echo intensity, are very dependent on the surrounding environment and target movements. Consequently, we have to extract training data set for each measurement in real-time to apply a supervised separation method. In this section, we first propose a real-time training data acquisition method from each imaging result based on the range profile. Then, we compare the separation performance of three representative supervised separation methods using the training data extracted by the proposed acquisition method. Based on these examinations, we propose an accurate image separation method for two adjacent pedestrians.

4.1 Proposed Training Data Acquisition Method

This section proposes a training data acquisition method for the supervised separation method of radar images. In our proposed method, the training data set consists of selected scattering centers from the estimated images using the range profiles. Figure 9 shows an example of a range profile when the peaks corresponding to two pedestrian targets have been detected. The first and second peaks correspond to Targets 1 and 2. The data between these peaks correspond to the in-
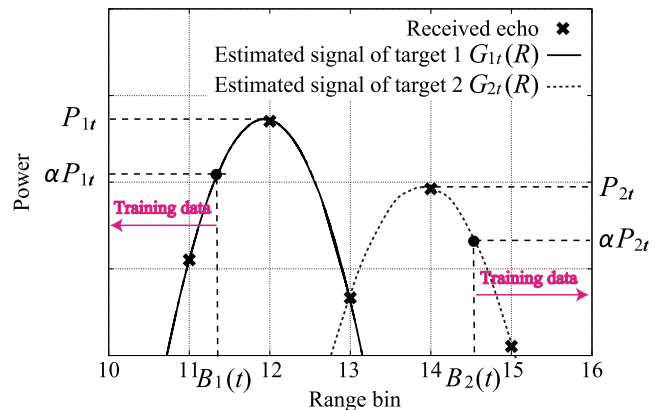
terference between the targets. Nevertheless, data on either side of these peaks can be regarded as echoes from one of the targets.

Based on the above consideration, training data are extracted for the scattering centers that exist around the peaks in the range profile. First, the two peaks of the range profile are extracted for each time bin t. Here, if two peaks cannot be acquired, training data are not extracted at time t. Next, it is assumed that the reflected signal from each target is a Gaussian function, and the signals shown in Fig. 9 are estimated using each peak and the two adjacent range gates around it. The estimated signal at t corresponding to Targets 1 and 2 are denoted as $G_{1t}(R)$ and $G_{2t}(R)$, and the maximum powers of $G_{1t}(R)$ and $G_{2t}(R)$ are denoted as P_{1t} and P_{2t}. A threshold is set for the acquisition of training data for Target 1 by the range for which $G_{1t}(R) = \alpha P_{1t}$ holds, where $0 < \alpha < 1$ is a constant. Consequently, the range threshold for Target 1 is determined from:

$$B_1(t) = \min\left(G_{1t}^{-1}(\alpha P_{1t})\right), \tag{9}$$

where G_{1t}^{-1} is the inverse function of G_{1t} and $\min(\cdot)$ is a function returning the minimum value. As shown in this equation and Fig. 9, α controls the threshold for the training data extraction, and its setting is important, both to avoid mislabeling the training data and to obtain a sufficient number of training data. A suitable setting for α is discussed in Sect. 5.2. For $B_1(t)$, scattering center information is extracted for the training data of Target 1 that satisfy the condition:

$$R(t, v_{dn}) < B_1(t). \tag{10}$$

The training data of Target 1 is (x_s, y_s, t) of the scattering centers extracted by this equation. Similarly, the threshold for Target 2 is determined by:

$$B_2(t) = \max\left(G_{2t}^{-1}(\alpha P_{2t})\right), \tag{11}$$

and the condition for training data extraction for Target 2 is:
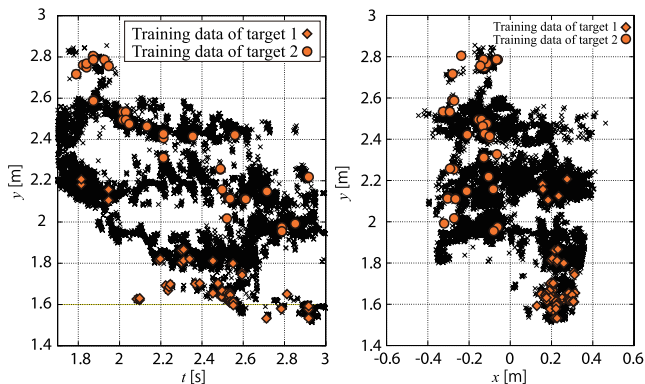
$$R(t, v_{dn}) > B_2(t). \tag{12}$$

Fig. 10 Top view and ty plane of the estimated image and acquired training data.

Fig. 11 Image separation result using 3-NN.

This training data acquisition process is conducted for a certain time interval T_{in}. All the data in T_{in} is used to acquire a labeled training data set $\psi_{tr} = (x_{tr}, y_{tr}, t_{tr})$.

Figure 10 shows the acquired training data with an α of 0.3 from the data of Fig. 6. As shown in this figure, a proper training data set can be extracted without label errors. Since there are only a limited number of time bins for which two peaks can be extracted, the amount of training data is small compared to the amount of estimated data. In this case, the ratio of training data to other data is 1.0%.

4.2 Selection of Appropriate Supervised Learning Method by Experiment

With a training data set with reliable labeling acquired using the method described in the previous section, we can use a supervised learning methods for image separation. This section selects an appropriate separation method from representative supervised classification methods by comparing their performance on experimental data. The feature space in these methods is xyt, the same as in Sect. 3.2.

4.2.1 K-Nearest Neighbor (k-NN)

The k-nearest neighbor (k-NN) algorithm is a simple and effective supervised separation method based on the closest training samples in the feature space [5], [19]. The procedure to separate the UWB Doppler radar images using this algorithm is:

1. Calculate the distance between an xyt of i-th unlabeled scattering center $\psi_i = (x_{si}, y_{si}, t_{si})$ and j-th training data ψ_{trj}. The distance is expressed as

$$D_{ij} = \sqrt{(x_{trj} - x_{si})^2 + (y_{trj} - y_{si})^2 + (t_{trj} - t_{si})^2}. \quad (13)$$

2. Distance D_{ij} is calculated for all training data.
3. Classify ψ_i to the the target label that most frequently appears in the k training vectors nearest to ψ_i selected with D_{ij}.

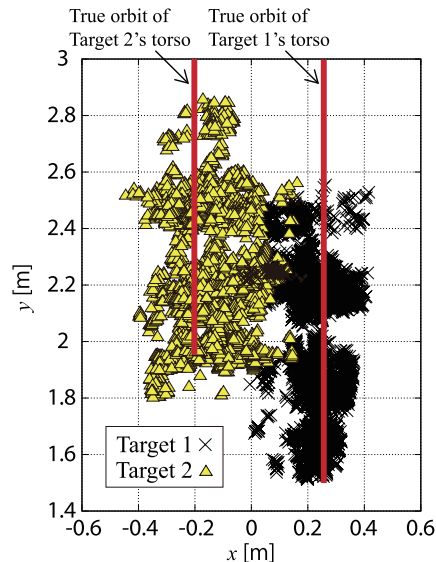Figure 11 shows the separation results for the 3-NN

with the same data as in Fig. 6. The data for $t > 1.5$ s are used, and $\alpha = 0.3$ is set empirically. The training data points are shown in Fig. 10, where the evaluation data consist of the other scattering points excluding the training data points. In this case, $k = 3$ is a better setting for k-NN. We can see that many scattering centers are accurately separated with a 3-NN method.

Here we quantitatively evaluate the separation accuracy. A separation error rate is defined using a true separation plane in xyt space, defined as the central plane between the assumed true orbits of the targets. The true orbit of Target l is expressed as $y = -t + y_l$ and $x = x_l$, and the true separation plane is defined as:

$$y_T(t, x) = -t - \frac{x_2 - x_1}{y_2 - y_1}x + \frac{y_1 + y_2}{2} \quad (14)$$

The number of misclassification points N_E using $y_T(t, x)$ are then counted and the separation error rate is defined as

$$\delta = N_E / N_{All}, \quad (15)$$

where N_{All} is the total number of estimated scattering centers. For the simple methods, δ of Fig. 6 and Fig. 8 are 18.4% and 20.1%, respectively. In contrast, δ of Fig. 11 is 10.3%, indicating that k-NN realizes a more accurate separation than the simple methods because it conducts a supervised learning method using training data extracted with the proposed acquisition method.

4.2.2 Naive Bayesian Classifier (NBC)

The Naive Bayesian classifier (NBC) is a probabilistic classifier based on Bayes' theorem with naive independence assumptions on the feature parameters [7], [20]. The probability model is

$$p(l|x_s, y_s, t) = \frac{p(l)p(x_s|l)p(y_s|l)p(t|l)}{p(x_s, y_s, t)}, \quad (16)$$
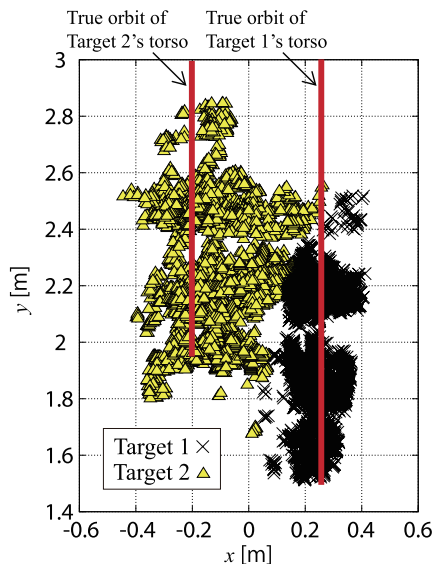
Fig. 12　Image separation result using NBC.

Fig. 13　Top view of the image separation result using SVM.

where $p(l|x_s, y_s, t)$ is the conditional probability of Target l given (x_s, y_s, t). These probability functions are calculated with the training data set [20], and the scattering centers are labelled according to the maximum a posteriori decision rule.

Figure 12 shows the classification results for the NBC algorithm with the same data as in Fig. 6. Here, NBC assumes the Gaussian distribution and the parameters are same as in the previous section. As shown in this figure, NBC generates many separation errors, especially near $(x, y) = (0.2\,\text{m}, 2.5\,\text{m})$ because it requires training data to be evenly distributed in the region where the data exists. The δ of Fig. 12 is 12.5%, worse than 3-NN because of these errors.

4.2.3　Support Vector Machine (SVM)

The SVM is an accurate classifier developed to create a non-linear separation boundary by applying the kernel technique [6], [21], [22]. The separating plane determined by a SVM is expressed as:

$$\sum_{i=1}^{N_{\text{Tr}}} w_i K(\psi_{\text{tr}}, \psi_{\text{tr}i}) + b = 0, \tag{17}$$

where w_i is a weight vector, b is the intercept, N_{Tr} is the number of training data, and $K(\mathbf{x}, \mathbf{x}') = \exp(-\sigma\|\mathbf{x} - \mathbf{x}'\|^2)$ is the Gaussian kernel function that is known as a general-purpose function for the SVM [21]. The parameters w_i and b are determined by a soft-margin optimization process [22]. The SVM parameters (σ and a parameter in the optimization process) are set by a grid search using the two-fold cross-validation approach [22].

Figure 13 shows the top view of the separation result using an SVM with the same data as in Fig. 6. As shown in this figure, a SVM achieves accurate separation. The separation error rate δ is 6.91%, better than 3-NN. This is because SVM needs only a small amount of training data near
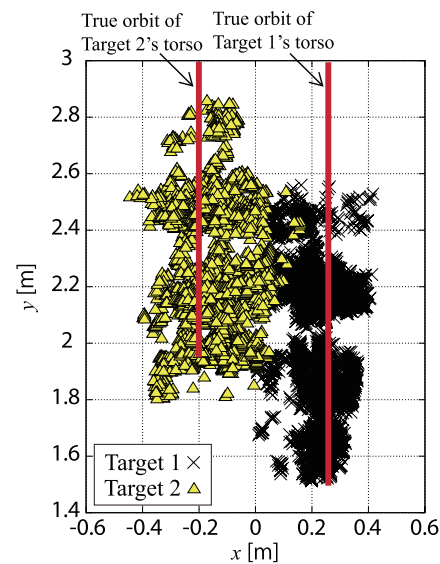
the class boundary for separation. In contrast, k-NN generally requires a larger number of training data points than SVM. Because the number of training data is small given the proposed training data acquisition method shown in Fig. 10, SVM is the most effective algorithm for the applications assumed in this paper. Hence, we selected SVM for the proposed separation method.

4.3　False Point Rejection

Image separation is achieved with the proposed training data acquisition method and SVM. However, because of the interference between targets, many false points that do not belong to either target remain near the separation boundary. As a final step, the proposed method removes these false points from the SVM separation results. First, a sphere centered at $\mathbf{x}_s(t, v_{dn})$ with a radius of r_b in the xyt_{wl} space is assumed, where $t_{wl} = tv_{wl}$ and v_{wl} is the mean radial velocity for the estimated scattering center corresponding to Target l ($l = 1, 2$). Next, the number N_l of scattering centers that belong to each target within the assumed sphere is counted. If it is assumed that $\mathbf{x}_s(t, v_{dn})$ belongs to Target 1, the scattering centers that satisfy the condition $N_1/N_2 < \beta$ are rejected as false points, where $0 < \beta < 1$ is empirically determined. If it is assumed that $\mathbf{x}_s(t, v_{dn})$ belongs to Target 2, the scattering centers that satisfy the condition $N_2/N_1 < \beta$ are rejected in the same way.

Figure 14 shows the top view of the separation result after applying the false point rejection method to Fig. 13. We set $r_b = \Delta R/10 = 3\,\text{cm}$, and $\beta = 0.3$ empirically. This figure indicates that some false points near the boundary are rejected. The δ of Fig. 14 is 4.87%, indicating that the proposed false point rejection method improves separation accuracy. In addition, Table 1 shows the δ for each method examined in Sect. 4, indicating that the combination of SVM and false point rejection realizes the best accuracy. Fig-
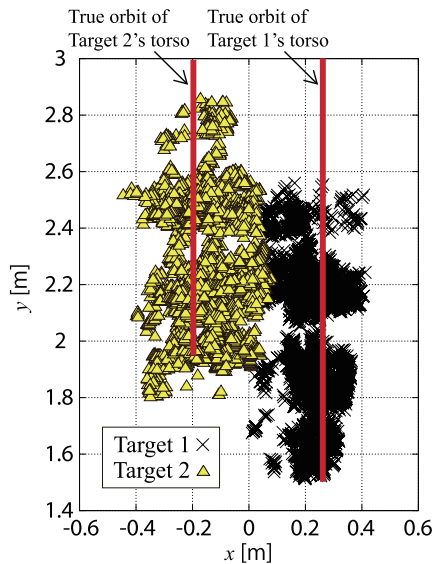
Fig. 14 Top view of the image separation result with the proposed method.

Table 1 The separation error rate δ of each method.

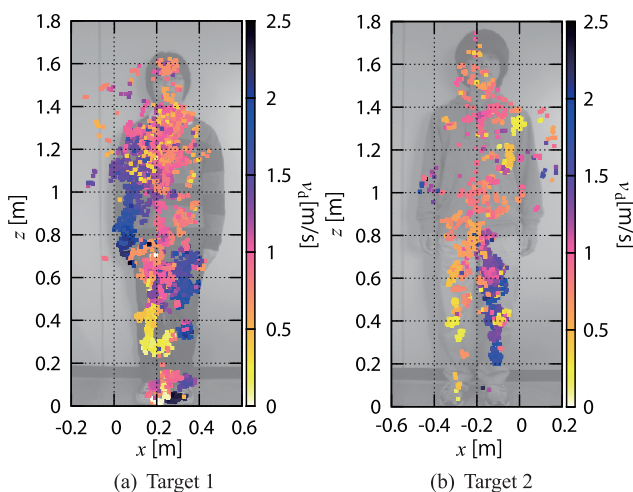|	without false point rejection	with the false point rejection
k-NN	10.3%	9.02%
NBC	12.5%	11.9%
SVM	6.91%	4.87%

(a) Target 1   (b) Target 2

Fig. 15 Frontal view of the image separated by the proposed method.

ure 15 shows that for $1.76\,\text{s} < t < 2.39\,\text{s}$, the frontal views of each image of Fig. 14 are well separated by this method. Although separation errors between targets still remain, the outlines of human shapes are observable. We can see from the v_d information that the left leg and the right arm of both targets are moving forward in this half of the walking cycle, a key feature of walking motion.

4.4 Procedure and Calculation Time

The procedure for the proposed image separation method is summarized as follows:

1. Estimate the scattering centers using each data of the time section whose length is T_{in}.
2. In each time section, obtain a training data set from these scattering centers using only the data for which two peaks of the range profiles can be extracted.
3. Determine the separation boundary with SVM using these training data.
4. Conduct separation using the determined boundary and false point rejection.
5. Iterate these steps until the end of the observation data is reached.

The separation processes, including training data acquisition, are conducted for each time interval T_{in}. In this study, T_{in} is set based on the gate cycle of the targets.

Here, we discuss the calculation time and real-time capability of the proposed method. As shown in above procedure, the proposed method requires the acquisition of training data set for each input data and determines the target label immediately after this process. Consequently, a sufficiently short-time input duration and fast calculation for both the training data extraction and the SVM algorithm are needed in practice. In the example shown in Fig. 14, T_{in} was 0.8 s, slightly longer than half the walking cycle, and the total calculation time for the training data acquisition and classification process was 0.33 s using an Intel Core i5-2520M CPU 2.50 GHz processor. This means that the proposed method has real-time capability.

5. Discussion

5.1 Performance Evaluation for Various Target Positions

In this subsection, the performance of the proposed separation method for various target positions is evaluated. Figure 16 shows the top view of the initial position of the targets. Here, the separation of the targets' torsos is $L = 67$ cm, and the relative positions are varied by angle θ. The range difference between the targets is changed by varying θ. For example, the range difference is small when θ is small where the same pedestrian targets as in the previous section are assumed. In all scenarios, the targets walk 2.4 m in a straight line, parallel to the y-axis towards the origin. The parameter α is empirically set for each θ, details of which are discussed in the next section. Other parameters and the experimental setup are the same as described in the previous section.

The relationships between θ and δ obtained from the separation methods examined in this paper (see Fig. 17) show that the separation accuracy of the proposed method is better for all θ. However, δ becomes comparatively large for $\theta = 0$ and 90°. When θ is nearly zero, the range difference between the targets is too small; therefore the extraction of training data is difficult in this case. When θ is nearly 90°, Target 2 is obscured by Target 1, and there is a considerable decrease in the number of estimated scattering centers for Target 2. However, with the exception of these cases, the
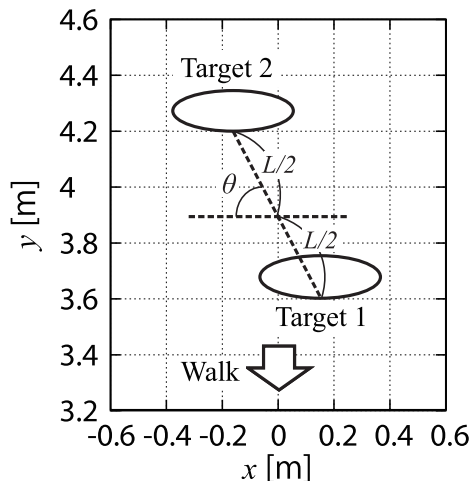
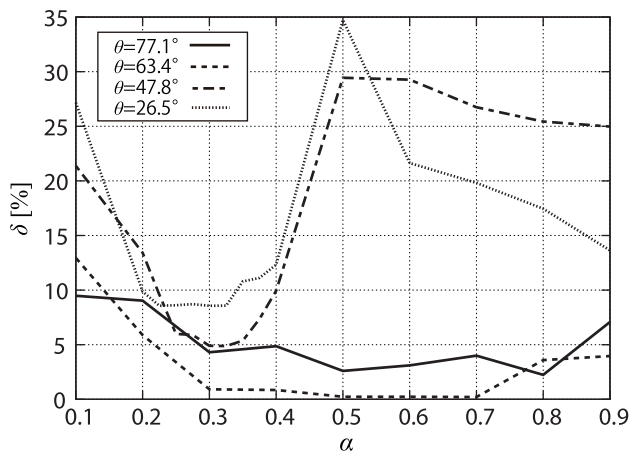**Fig. 16** Top view of initial positions of the targets.
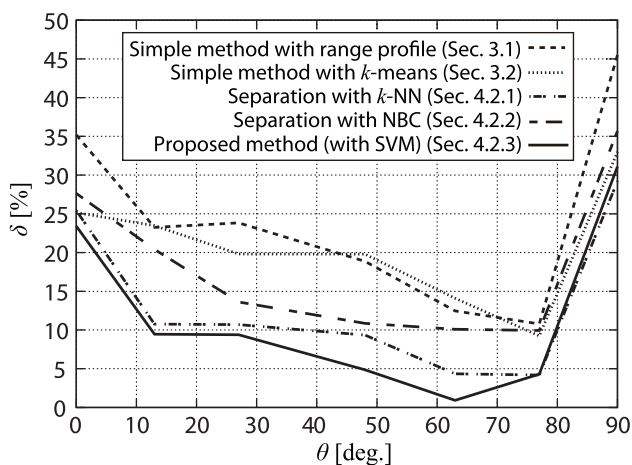

Fig. 18 Relationship between α and δ.

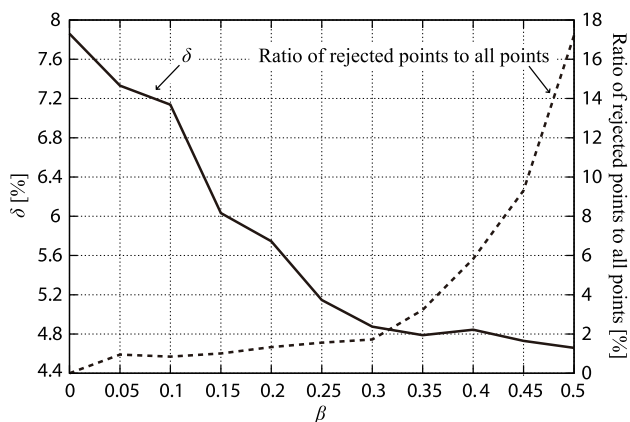**Fig. 17** Separation error rate for various target positions.

Fig. 19 Relationship between β, δ, and the ratio of rejected points to all estimated points.

proposed method achieves an accurate separation over the interval $10° < \theta < 80°$. These results verify that the proposed separation method works well for various positions of pedestrians.

5.2 Suitable Parameters for α and β

This section investigates suitable settings for the parameters α and β. First, α is discussed. Equations (9) and (11) show that α determines the threshold of training data acquisition and the separation accuracy depends on the amount of training data. On one hand, if α is set too small, the amount of training data becomes insufficient. On the other hand, if α is too large, an improper training data set is extracted because of interference from the targets. For these reasons, setting the correct α value is important for the proposed method. To investigate suitable values for α, the relationship between α and the separation accuracy for the various target positions assumed in the previous section was estimated.

The separation error rate δ for each α and θ (see Fig. 18) shows that the optimum values for α depend on the relative

positions of the targets. When θ is small, the appropriate α also needs to be small because there is an increase in training data extraction errors for larger α. In contrast, the optimum α value can be relatively large for large θ. Sufficiently accurate separation is achieved at $\alpha = 0.3$ for all θ, hence this is a suitable setting for a wide range of situations. However, when the range separation between the targets is sufficiently large, the separation accuracy can be improved by setting larger α values. Thus, a suitable α can be chosen based on the range difference between targets. For example, when the mean range difference between targets estimated in the training data acquisition process is larger than $2\Delta R$, a value of $\alpha = 0.6$ is appropriate. In other cases where the range difference is relatively small, we set $\alpha = 0.3$.

Next, the parameter β, the threshold in the false point rejection method, is discussed. If β is too large, too many points are rejected. Conversely, if β is set small, many false points near the separation boundary remain. For these reasons, the relationships among $\beta - \delta$, β, and the number of rejected points are important for the appropriate setting of β. Figure 19 shows these relationships for $\theta = 47.8°$ and $\alpha = 0.3$. The classification accuracy is improved when β is

large. However, the number of rejected points become excessive when $\beta > 0.4$. Moreover, the improvement in δ is relatively small when $\beta > 0.25$. Based on these observations, the interval $0.25 < \beta < 0.35$ is a suitable setting. In addition, the same tendency for the other parameter θ is confirmed. Thus, $\beta = 0.3$ is a suitable setting for all situations assumed in this paper.

6. Conclusions

A UWB Doppler radar-based image separation method for two closely spaced pedestrians was proposed in this paper. Its accuracy was demonstrated by the applications in realistic environments. First, simple image separation using unsupervised methods were tested and it was experimentally shown that the separation accuracy of adjacent pedestrians was inadequate. To achieve better accuracy, an image separation method using supervised learning trained on the obtained data itself from range profiles was proposed. The experiments that involved two pedestrians separated by 0.44 m walking towards the radar compared the separation performance of several representative supervised separation methods (k-NN, NBC, and SVM), and clarified the effectiveness of the SVM compared to other methods. With a down-range resolution of 0.3 m, the features of the pedestrians were evident from images separated by the proposed method. The separation error rate for the proposed separation methods was 4.87%. In addition, the input time duration for each separation process was 0.8 s and the total calculation time for training data acquisition and classification processes was 0.33 s. These results verify that the proposed method achieves accurate and real-time separation of pedestrians in close proximity. Finally, the performance and parameters of the proposed method for various relative positions of the pedestrians were also examined, and a suitable parameter setting was established for the proposed method that optimizes the SVM training process. Investigation of the separation of more than two closely spaced targets and the combination of the proposed method and target number estimation are important future tasks.

Acknowledgments

References

[1] Y. Wang, Q. Liu, and A.E. Fathy, "CW and pulse-doppler radar processing based on FPGA for human sensing applications," IEEE Trans. Geosci. Remote Sens., vol.51, no.5, pp.3097–3107, 2013.

[2] O.R. Fogle and B.D. Rigling, "Micro-range/micro-Doppler decomposition of human radar signatures," IEEE Trans. Aerosp. Electron. Syst., vol.48, no.4, pp.3058–3072, 2012.

[3] A. Sume, M. Gustafsson, M. Herberthson, A. Jänis, S. Nilsson, J. Rham, and A. Örbom "Radar detection of moving targets behind corners," IEEE Trans. Geosci. Remote Sens., vol.49, no.6, pp.2259–2267, 2011.

[4] I. Orović, S. Stanković, and M. Amin, "A new approach for classification of human gait based on time-frequency feature representations," Signal Process., vol.91, no.6, pp.1448–1456, 2011.

[5] G.E. Smith, W. Karl, and C.J. Baker, "Radar micro-Doppler signature classification using dynamic time warping," IEEE Trans. Aerosp. Electron. Syst., vol.46, no.3, pp.1078–1096, 2010.

[6] Y. Kim and H. Ling, "Human activity classification based on micro-Doppler signatures using a support vector machine," IEEE Trans. Geosci. Remote Sens., vol.47, no.5, pp.1328–1337, 2009.

[7] I. Bilik and J. Tabrikian, "Radar target classification using Doppler signatures of human locomotion models," IEEE Trans. Aerosp. Electron. Syst., vol.43, no.4, pp.1510–1522, 2007.

[8] T. Thayaparan, S. Abrol, E. Riseborough, L. Stankovic, D. Lamothe, and G. Duff, "Analysis of radar micro-Doppler signatures from experimental helicopter and human data," Inst. Eng. Tech. Radar Sonar Navig., vol.1, no.4, pp.289–299, 2007.

[9] J.A. Hogbom, "Aperture synthesis with a non-regular distribution of interferometer baselines," Astron. Astrophys. Suppl. Ser., vol.15, pp.417–426, 1974.

[10] S. Chang, R. Sharan, M. Wolf, N. Mitsumoto, and J.W. Burdick, "People tracking with UWB radar using a multiple-hypothesis tracking of clusters (MHTC) method," Int. J. Soc. Robot., vol.2, pp.3–18, 2010.

[11] A. Lin and H. Ling, "Doppler and direction-of-arrival (DDOA) radar for multiple-mover sensing," IEEE Trans. Aerosp. Electron. Syst., vol.43, no.4, pp.1496–1509, 2007.

[12] A. Lin and H. Ling, "Three-dimensional tracking of humans using very low-complexity radar," Electron. Lett., vol.42, no.18, pp.1062–1063, 2006.

[13] T. Sakamoto, Y. Matsuki, and T. Sato, "Method for the three-dimensional imaging of a moving target using an ultra-wideband radar with a small number of antennas," IEICE Trans. Commun., vol.E95-B, no.3, pp.972–979, March 2012.

[14] Z. Zeng, J. Sun, and F. Liu, "Through-wall detection of human being's movement by UWB radar," IEEE Geosci. Remote Sens. Lett., vol.9, no.6, pp.1079–1083, 2012.

[15] T. Sakamoto and T. Sato, "Two-dimensional ultra-wide-band radar imaging of a target with arbitrary translation and rotation," IEEE Trans. Geosci. Remote Sens., vol.49, no.11, pp.4493–4502, 2011.

[16] W. Shiyou, X. Yanyun, C. Jie, M. Shengwei, F. Guangyou, and Y. Hejun, "A new method of through wall moving target detection and imaging using UWB-SP radar," Proc. 2011 IEEE Int. Geoscience and Remote Sensing Symp. (IGARSS), pp.182–185, 2011.

[17] K. Saho, T. Sakamoto, T. Sato, K. Inoue, and T. Fukuda, "Pedestrian imaging using UWB Doppler radar interferometry," IEICE Trans. Commun., vol.E96-B, no.2, pp.261–266, Feb. 2013.

[18] K. Saho, T. Sakamoto, T. Sato, K. Inoue, and T. Fukuda, "Experimental study of real-time human imaging using UWB Doppler radar interferometry," Proc. 6th European Conf. Antennas and Propagation (EuCAP2012), Prague, Chech Republic, M16-3, 2012.

[19] T.M. Cover and P.E. Hart, "Nearest neighbor pattern classification," IEEE Trans. Inf. Theory, vol.13, no.1, pp.21–27, 1968.

[20] S. Kotsiantis and P. Pintelas, "Increasing the classification accuracy of simple bayesian classifier," Springer-Verlag Lecture Notes in Artificial Intelligence, vol.3192, pp.198–207, 2004.

[21] C.J.C. Burges, "A tutorial on support vector machines for pattern recognition," Data mining and knowledge discovery, vol.2, no.2, pp.121–167, 1998.

[22] C.L. Huanga, M.C. Chenb, and C.J. Wangc, "Credit scoring with a data mining approach based on support vector machines," Expert Systems with Applications, vol.33, no.4, pp.847–856, 2007.

[23] E. Jacobsen and R. Lyons, "The sliding DFT," IEEE Trans. Signal Process. Mag., vol.20, no.2, pp.74–80, 2003.

[24] R. Pickholts, D. Schilling, and L.B. Milstein, "Theory of spread-spectrum communications-A tutorial," IEEE Trans. Commun., vol.COM-30, pp.855–882, 1982.

[25] T. Fukuda, N. Nagoro, S. Ujita, S. Nagai, M. Nishijima, H. Sakai,

T. Tanaka, and D. Ueda, "A 26 GHz short-range UWB vehicular radar using 2.5 Gcps spread spectrum modulation," IEEE/MTT-S International Microwave Symposium 2007, pp.1311–1314, 2007.

[26] E.W. Forgy, "Cluster analysis of multivariate data: Efficiency versus interpretability of classifications," Biometrics, vol.21,pp.768–769, 1965.

[27] J.H. Ward, Jr., "Hierarchical grouping to optimize an objective function," J. American Statistical Association, vol.58, pp.236–244, 1963.

Toru Sato received his B.E., M.E., and Ph.D. degrees in electrical engineering from Kyoto University, Kyoto, Japan in 1976, 1978, and 1982, respectively. He has been with Kyoto University since 1983 and is currently a Professor in the Department of Communications and Computer Engineering, Graduate School of Informatics. His major research interests include system design and signal processing aspects of UWB radars, atmospheric radars, radar remote sensing of the atmosphere, and radar observation of space debris. He is a member of the Institute of Electrical and Electronics Engineers, the Society of Geomagnetism and Earth, Planetary and Space Sciences, the Japan Society for Aeronautical and Space Sciences, and American Meteorological Society.

Kenshi Saho received his B.E. degree from Kyoto University in 2008 and M.I. and Ph.D. degrees from the Graduate School of Informatics, Kyoto University, in 2010 and 2013, respectively. He is currently a Research Fellow of the Japan Society for the Promotion of Science (JSPS) with the Department of Communications and Computer Engineering, Graduate School of Informatics, Kyoto University. His current research interest is in signal processing and pattern recognition for UWB radars. He is a member of the IEEJ.

Hiroaki Homma received the B.E. degree in Electrical and Electronic Engineering from Kyoto University in 2010 and the M.I. degree in Informatics from Kyoto University in 2012. His research interest was in UWB Doppler imaging radar. In 2012, he joined KDDI Corporation.

Kenichi Inoue received the B.S. and M.S. degrees in electronic science and engineering from Kyoto University, Kyoto, Japan, in 2000 and 2002, respectively. In 2002, he joined Semiconductor Device Research Center, Semiconductor Company, Matsushita Electric Industrial Co. Ltd., Osaka, Japan, where he was working on semiconductor laser devices, sensor devices and sensor systems. Since 2009, he has been with Advanced Technology Research Laboratories, Panasonic Corporation, Kyoto, Japan, where he is involved in the research and development of UWB radar sensor system and its applications. Mr. Inoue is a member of the Japan Society of Applied Physics and the Institute of Electronics, Information and Communication Engineers of Japan.

Takuya Sakamoto received his B.E. degree from Kyoto University in 2000, and M.I. and Ph.D. degrees from the Graduate School of Informatics, Kyoto University in 2002 and 2005, respectively. He is an assistant professor in the Department of Communications and Computer Engineering, Graduate School of Informatics, Kyoto University. His current research interest is in UWB radar signal processing. He is a member of the IEEJ and the IEEE.

Takeshi Fukuda was born in Osaka, Japan, in 1969. He received the B.S. and M.S. degrees in Electronic Engineering from Osaka University, Suita, Japan, in 1993 and 1995, respectively. In 1995, he joined the Electronics Research Laboratory, Matsushita Electronics Corporation, Osaka, Japan, where he has been engaged in the research and development of microwave integrated circuits. Since 2009, he has been with Advanced Technology Research Laboratories, Panasonic Corporation, Kyoto, Japan. His current research interests are algorithms and RF architectures for high-resolution millimeter-wave radar systems.